

Gap dependence of the tip-sample capacitance

Shu Kurokawa and Akira Sakai

Citation: *Journal of Applied Physics* **83**, 7416 (1998); doi: 10.1063/1.367985

View online: <http://dx.doi.org/10.1063/1.367985>

View Table of Contents: <http://scitation.aip.org/content/aip/journal/jap/83/12?ver=pdfcov>

Published by the AIP Publishing

Articles you may be interested in

[Analysis of capacitive force acting on a cantilever tip at solid/liquid interfaces](#)

J. Appl. Phys. **113**, 154311 (2013); 10.1063/1.4801795

[X-ray nanotomography of SiO₂-coated Pt₉₀Ir₁₀ tips with sub-micron conducting apex](#)

Appl. Phys. Lett. **99**, 173102 (2011); 10.1063/1.3655907

[ac driving amplitude dependent systematic error in scanning Kelvin probe microscope measurements: Detection and correction](#)

Rev. Sci. Instrum. **77**, 043711 (2006); 10.1063/1.2195104

[STMInduced Luminescence Spectra from Au\(111\) with STM Tips of PtIr Alloys](#)

AIP Conf. Proc. **696**, 927 (2003); 10.1063/1.1639804

[Tip-sample capacitance in capacitance microscopy of dielectric films](#)

J. Appl. Phys. **84**, 4043 (1998); 10.1063/1.368617

The advertisement features a blue background with a film strip graphic on the left. The text is in white and orange. The main headline reads 'Not all AFMs are created equal' in orange, followed by 'Asylum Research Cypher™ AFMs' in white, and 'There's no other AFM like Cypher' in orange. Below this is the website 'www.AsylumResearch.com/NoOtherAFMLikeIt' in white. In the bottom right corner is the Oxford Instruments logo, which consists of the word 'OXFORD' above 'INSTRUMENTS' inside a square frame, with the tagline 'The Business of Science®' below it.

Not all AFMs are created equal

Asylum Research Cypher™ AFMs

There's no other AFM like Cypher

www.AsylumResearch.com/NoOtherAFMLikeIt

OXFORD
INSTRUMENTS
The Business of Science®

Gap dependence of the tip-sample capacitance

Shu Kurokawa^{a)} and Akira Sakai

Mesosopic Materials Research Center, Kyoto University, Sakyo-ku, Kyoto 606-01, Japan

(Received 12 January 1998; accepted for publication 12 March 1998)

The tip-sample capacitance has been studied in the nontunneling regime and the capacitance-distance characteristics and its dependence on the tip geometry have been determined for the gap distance $1 < s < 600$ nm. Measurements were carried out in ultrahigh vacuum on a capacitor formed between a metal tip (W or Pt-Ir) and a clean Au(111) surface. Tips of different tip radius $R = 30 \sim 4000$ nm were used to investigate the influence of tip geometry on the capacitance. When the gap distance is reduced, the capacitance increases while its gap sensitivity $|\partial C/\partial s|$ decreases with the gap distance. The capacitance therefore shows no $1/s$ divergence. The magnitude of the capacitance change is found to depend on the tip geometry: blunt tips ($R > 1000$ nm) show larger capacitance increase than that for sharp tips ($R \leq 100$ nm). The effective tip radius R_{eff} estimated from the $C-s$ characteristics agrees with the real tip radius in a limited distance range which varies with the tip geometry. At small distances ($s < 30$ nm), $R_{\text{eff}} \approx R$ for sharp tips but $R_{\text{eff}} < R$ for blunt tips. On the other hand at large distances ($s > 200$ nm), the relation is reversed, $R_{\text{eff}} > R$ for sharp tips while $R_{\text{eff}} \sim R$ for blunt tips. These results on R_{eff} can be explained by the field concentration to the tip apex and the change of capacitance-contributing tip area with the gap distance. Capacitance calculations indicate that the capacitance of the “truncated cone + half sphere” tip well reproduces the observed $C-s$ characteristics and its dependence on the tip geometry. © 1998 American Institute of Physics. [S0021-8979(98)05012-9]

I. INTRODUCTION

Tip-sample capacitance at a gap distance less than $1 \mu\text{m}$ plays an important role in various scanning probe microscopies (SPMs). In the scanning capacitance microscopy (SCaM),^{1–10} for example, the tip-sample capacitance is just the quantity to be measured with. Also the capacitance force between the tip and the sample gives a major contribution to the attractive tip-sample force in the electrostatic and related force microscopies.^{11–15} Recent experiments^{16,17} with ultrahigh-vacuum noncontact atomic force microscopy (UHV NC-AFM) shows that the capacitance force makes non-negligible effects in the atom-resolved AFM imaging of surfaces. Electron tunneling in scanning tunneling microscopy (STM) is also influenced by the tip-sample capacitance. Coulomb blockade in STM junctions is a well known example.^{18–26} In these Coulomb blockade experiments, the capacitance charging between the STM tip and a small particle (or an island) on a substrate controls the electron tunneling. The capacitance also effects the tunneling dynamics since the time constant of electron tunneling in STM is determined by the tip-sample capacitance and the tunneling resistance. This role of the capacitance has turned out to be quite important in recent experiments on ultrafast STM.^{27–30}

In spite of a variety of its roles in SPMs, little has been known on the basic characteristics of the tip-sample capacitance. For example, no direct experimental data is available on how the capacitance changes with the gap distance s and how it behaves in the nanometer-scale proximity regime where some mesoscopic effects in capacitance^{31–33} might be

expected. In many cases, the tip-sample system is treated as a parallel-plate capacitor and the simple $1/s$ behavior is assumed for its capacitance. At small separations of tens of nanometer or less, however, the planar capacitor model cannot necessarily be a good approximation for the real tip-sample geometry and the $1/s$ divergence may not be an obvious gap dependence for the tip-sample capacitance. Experimental information on the capacitance at $s \ll 1 \mu\text{m}$ is, however, quite controversial, and various SPM experiments predict a different gap dependence. In their topographic SCaM experiment, Kleinknecht *et al.*⁴ employed the spherical tip model (tip radius R) and showed that at $s < R$ the tip-sample capacitance has the gap sensitivity $\partial C/\partial s = 2\pi\epsilon_0 R/s$, which by integrating with s leads to $C = 2\pi\epsilon_0 R \ln(8R/s)$. This logarithmic dependence of the SCaM capacitance is experimentally observed down to 100 nm.³⁴ Further information, however, has not been obtained from SCaM since recent contact-type SCaM^{5–10} is concerned with the capacitance–voltage ($C-V$) characteristics and operated at a constant tip-sample separation. The gap sensitivity $\partial C/\partial s$ is also proportional to the capacitance tip-sample force which can be directly measured in electrostatic force microscopy (EFM). Martin *et al.*¹¹ carried out the force measurements down to $s \sim 2$ nm and find that the parallel-plate capacitor of area $(0.14 \mu\text{m})^2$ gives a good agreement with experiment. Their measurements thus indicate $C \propto 1/s$. On the other hand, Yokoyama *et al.*¹⁴ have reported that their force data are well represented by the relation $\partial C/\partial s \propto \ln s$. They also showed theoretically that the capacitive force between a conical tip and a plane varies logarithmically with s . This gives a nondivergent capacitance $C = C_0 - P_0 s [1 + \ln(D/s)]$, where C_0 , P_0 , and D are constants.

^{a)}Electronic mail: kurokawa@mesostm.mtl.kyoto-u.ac.jp

Therefore previous SCA and EFM experiments predict three different gap dependences for the tip-sample capacitance.

Controversy in the tip-sample capacitance also exists in the tunneling regime. STM-based Coulomb blockade experiments^{18,21–23} consistently give the capacitance which varies as $1/s$. On the other hand, the “quantum” capacitance obtained in the ultrafast STM experiment of Weiss *et al.*²⁷ is proportional to the tunneling resistance and is thus expressed as $C = C_0 \exp(-\kappa s)$ with constants C_0 and κ . This quantum capacitance agrees with the theoretical mesoscopic capacitance^{31–33} which also varies linearly with the junction resistance. However subsequent ultrafast STM experiments^{28,29} have questioned the quantum capacitance and revealed that the transient behavior of the tunneling current is governed by the usual geometrical capacitance. Another problem of the capacitance in the tunneling regime is its small magnitude (0.1–1 aF) compared with larger capacitance values (10–100 aF) obtained from the SCA and EFM measurements in the nontunneling regime. If we assume a single $C-s$ characteristic, this difference in the capacitance values would lead to a few orders of magnitude mismatch at the transition from the nontunneling to the tunneling regime. A possible solution to this problem is to distinguish the two capacitances; the “electrochemical” capacitance relevant to the electron tunneling and the usual geometrical capacitance, as suggested by Büttiker and his co-workers.^{31–33} According to their theory, the electrochemical capacitance in the Coulomb blockade experiments can take small values even when the geometric capacitance is much larger. However, the small capacitance in the Coulomb blockade experiments can be explained as well by the small size of the charging electrodes. It is therefore not clear at present whether the experimental capacitance in the tunneling regime is electrochemical or geometrical and how it is related to the capacitance in the nontunneling regime.

In this article we report our experimental study of the tip-sample capacitance for a wide range of the gap distance down to the onset of electron tunneling. The aim of this study is to establish the gap dependence of the capacitance in the nontunneling regime with particular emphasis on the effect of tip geometry. We have already carried out some measurements on the tip-semiconductor capacitance.^{35,36} This study is an extension of our capacitance measurements to a metal surface. Since metal surfaces have no space charge layers, the genuine behavior of the tip-sample capacitance is expected to be obtained. In Sec. II we describe our capacitance measurements. The observed gap dependence of the tip-sample capacitance and its relation to the tip geometry are presented and discussed in Sec. III. Our experimental results are compared with the simulated tip-sample capacitance in Sec. IV and with the capacitance predicted by other SPM experiments in Sec. V.

II. EXPERIMENTAL SETUP

The experiment was performed in an ultrahigh vacuum chamber with a homemade STM system. The chamber base pressure was 2×10^{-8} Pa. The sample used in this experi-

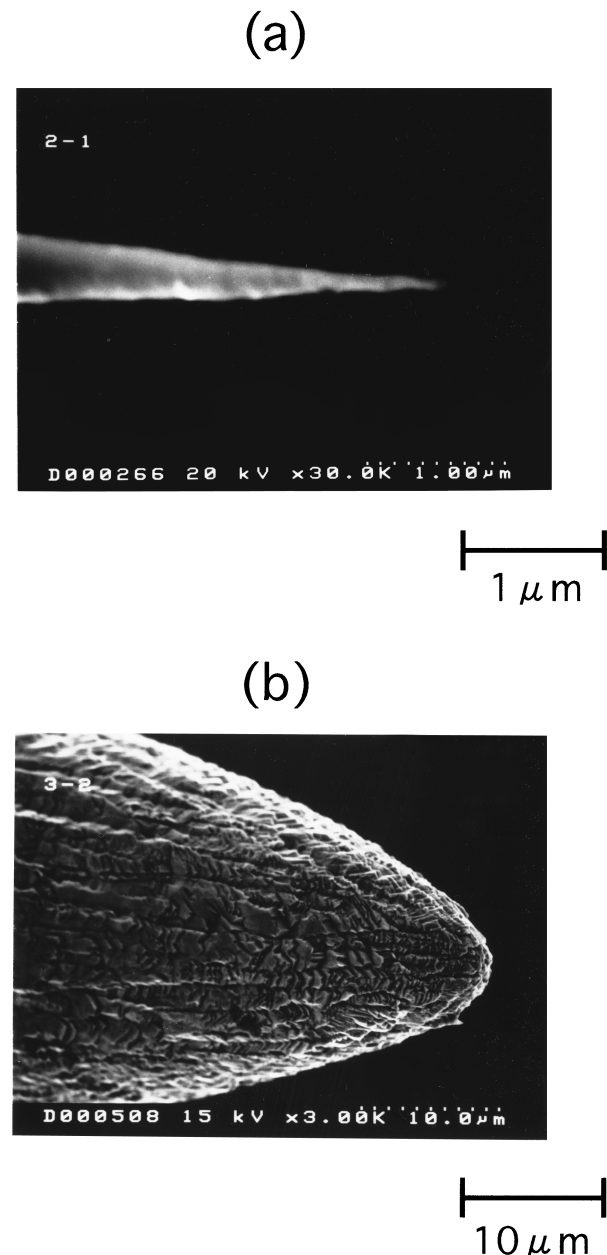


FIG. 1. SEM micrographs of the tungsten tip (a) and the blunt platinum-iridium tip (b). Note the difference in scale bars. The tip radius R is 30 nm for the tungsten tip while $R \sim 4000$ nm for the platinum-iridium tip.

ment was a gold film deposited on a sapphire substrate. The gold deposition was made in an auxiliary chamber by heating a tungsten filament. After transferring the sample into the STM chamber, the sample was first heated at around 570 K for ~ 1000 s. A clean (111) surface is routinely obtained with this annealing procedure. Electropolished tungsten (W) and platinum-iridium (Pt-Ir) tips were used in the STM imaging and in the capacitance measurements. These tips were inspected by scanning electron microscope (SEM) and the tip radius was estimated from the SEM micrographs. Figure 1 shows the SEM micrographs of the W and Pt-Ir tips used in this experiment. The W tips have a sharp apex with a tip radius $R = 30$ –100 nm, while the Pt-Ir tips show a blunt end form with $R = 2000$ –4000 nm. Since the geometry of the

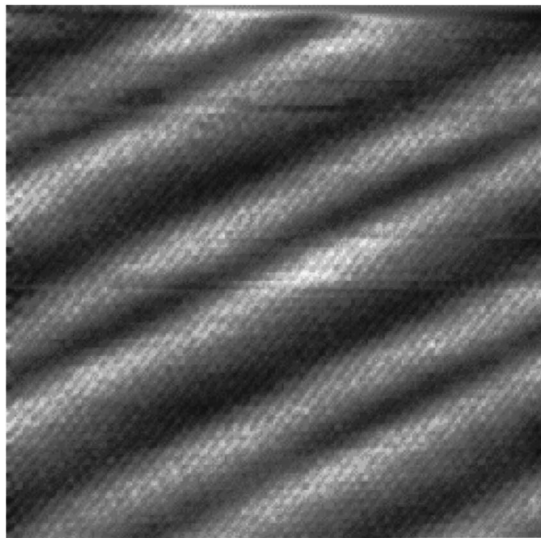


FIG. 2. STM micrograph of the gold film surface. The image size is 22 nm \times 22 nm. Pairs of parallel corrugation lines, characteristic of the $23 \times \sqrt{3}$ reconstruction of the clean Au(111) surface, are clearly observed.

blunt tips is not perfectly spherical, their R values are subjected to a large uncertainty of about 200 nm. These SEM pictures were used to prepare tips of different tip radii ranging from 30 to 4000 nm. This enables us to investigate the influence of tip geometry on the tip-sample capacitance, as will be described in Sec. III B.

Prior to every capacitance measurement, the gold film surface was first observed with STM to ensure that the sample surface is sufficiently smooth and free from contamination. Usually the STM image shows a few flat terraces bounded by atomic height steps. A typical STM image of the terrace is shown in Fig. 2. Pairs of parallel corrugation lines, constructing the $23 \times \sqrt{3}$ herringbone reconstruction of the clean Au(111) surface, are clearly observed. The STM image was normally acquired at a tunneling current of 0.5 nA and a bias voltage of 30 mV. After STM imaging, the tip was slightly retracted to a position corresponding to a current of ~ 50 pA. Then the electric connections to the tip and the sample were switched from the STM electronics to an ac capacitance bridge (Andeen Hagerling 2500 A), and the capacitance measurement was started. The bridge was operated at 1 kHz with an excitation voltage of $0.75 V_{\text{rms}}$. We changed the excitation voltage and found no systematic influence on the measured capacitance. The accuracy of the capacitance is ~ 2 aF after averaging eight readings.

We note that the absolute magnitude of the tip-sample capacitance is of little physical significance because the tip-sample junction is shunted by a huge stray capacitance, which is approximately 0.5 pF in our STM. This stray capacitance arises from the leads and other macroscopic parts of the tip-sample junction and does not change when the tip moves less than 1 μm . In each measurement with several cycles of tip approaching and tip retraction, the stray capacitance measured at large gap distances remains unchanged within ± 4 aF. Therefore the *relative change* in the measured capacitance with the gap distance represents the change in the tip-sample capacitance. The magnitude of this capaci-

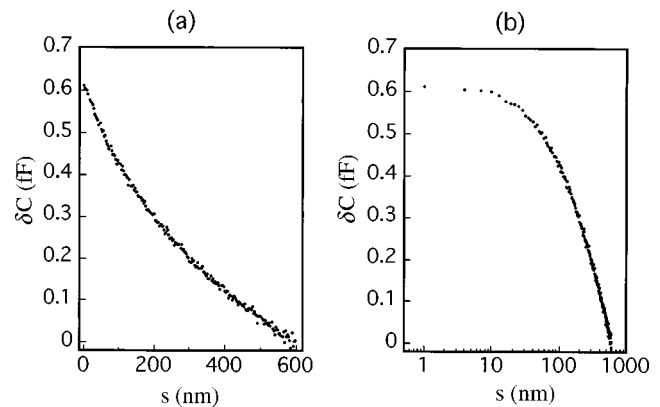


FIG. 3. Relative increase in the tip-sample capacitance δC as a function of the gap distance, plotted in a linear distance scale (a) and in a logarithmic scale (b). δC is measured from the capacitance value at 600 nm. This data were taken with the platinum-iridium tip shown in Fig. 1(b).

tance change is much smaller than the stray capacitance but it is still large enough to be detected with the ac bridge.

The tip motion above the tunneling distance was controlled by an inchworm motor. The displacement of the inchworm motor was calibrated against the piezo scanner which, in turn, was calibrated against the step height of Si(111). The overall accuracy of our distance scale is 10%. In order to avoid tip crashing, the capacitance was always measured while retracting the tip from the tunneling position. The initial tip-sample separation in the capacitance measurements is thus the tunneling distance at which the tunneling conductance is approximately 1.7 nS. We assume this gap distance to be 1 nm and use this value as a reference point of the distance scale. Although the actual tunneling gap cannot be known accurately, it cannot be much different from 1 nm because of the large gap sensitivity of the tunneling conductance. According to the semiclassical model³⁷ of the electron tunneling from the hemispherical tip, the tunneling conductance 1.7 nS corresponds to the gap distance of 0.8–0.9 nm. Therefore the offset of our distance scale is considered to be less than 0.5 nm. Since most capacitance data were taken at distances larger than 5 nm, this small offset makes negligible effects on the observed capacitance-distance characteristics.

III. EXPERIMENTAL RESULTS AND DISCUSSION

A. Gap dependence

In Figs. 3(a) and 3(b), we show the measured capacitance in a linear distance scale and in a logarithmic distance scale, respectively. To eliminate the contribution from the stray capacitance, the relative change δC defined by $\delta C = C - C(s = 600 \text{ nm})$ is plotted in these figures. The zero of δC is arbitrarily chosen at 600 nm. In Fig. 3(a), the capacitance continuously increases as the gap distance is reduced and appears to diverge as $1/s$. However, the measured gap dependence is quite different from $1/s$ as seen in Fig. 3(b). For $s > 200$ nm, the capacitance appears to change almost linearly with $\ln s$. Then the slope of the $\delta C - \ln s$ curve becomes gradually suppressed as the gap distance is further reduced, and the capacitance shows a weak gap dependence at $s < 50$ nm. It should be noted that the capacitance does not

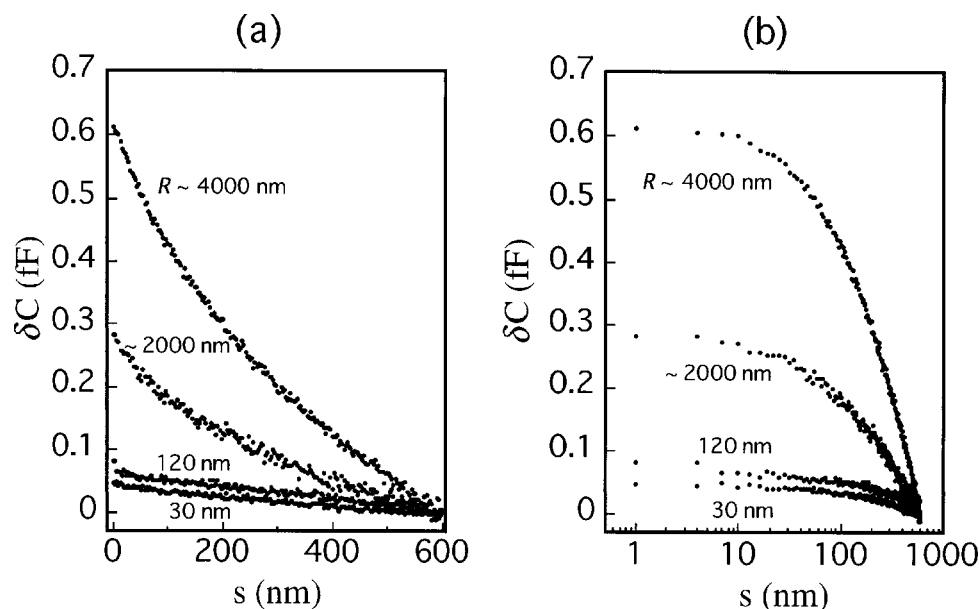


FIG. 4. $\delta C-s$ (a) and $\delta C-\ln s$ (b) characteristics obtained with tips of different sharpness. The values of SEM tip radius are also indicated in the figure. It can be seen that the tip radius has much influence on the total increment of the capacitance.

actually saturate at small distances but still increases as shown in Fig. 3(a). Its rate of increase $|\partial C/\partial s|$, however, decreases with the gap distance. If the capacitance changes as $1/s$, the rate $|\partial C/\partial s|$ should diverge as $1/s^2$ when $s \rightarrow 0$. This is just the opposite of the observed behavior. Figure 3(b) clearly indicates that the tip-sample capacitance diverges no faster than $\ln s$. It is also worth noting that the capacitance shows no anomalous behavior as the tip approaches the tunneling regime. Quantum effects in capacitance, even if they exist, are not observed at least down to ~ 1 nm.

The capacitance data in Fig. 3 were taken with a Pt-Ir tip. Similar $\delta C-\ln s$ characteristics were also obtained with other tips. In particular, the almost linear behavior at $s > 200$ nm and the apparent saturation at $s < 50$ nm are commonly observed for all tips. However, the total change in δC through $1 < s \leq 600$ nm is found to depend on the tip geometry. This will be discussed in Sec. III B.

We note that the $\delta C-\ln s$ curves [the same as the one shown in Fig. 3(b)] have been observed previously in our studies of the tip-semiconductor capacitance.^{35,36} In Ref. 36, we showed that the capacitance formula $C = C_0 - P_0 s [1 + \ln(D/s)]$ for the conical tip model¹⁴ gives a good fit to the experimental $\delta C-\ln s$ curves. However we later found³⁸ that the obtained parameters P_0 and D , which are related to the cone angle and the axial length of the conical tip, respectively, are not consistent with the actual tip geometry. This failure of the conical tip model urged us to study more systematically the role of tip geometry in the tip-sample capacitance.

B. Effect of tip geometry

We measured the capacitance using tips of various tip radius ranging from 30 to 4000 nm and obtained the $\delta C-s$ characteristics shown in Fig. 4. As in Fig. 3, the

$\delta C-s$ curves are represented in both linear [Fig. 4(a)] and logarithmic [Fig. 4(b)] distance scales. The relative change δC is again defined as the capacitance change from its value at $s = 600$ nm so that all curves in Fig. 4 merge at this distance. Comparison of these curves in Fig. 4 clearly indicates a strong influence of the tip radius on the capacitance. Quantitatively, all $\delta C-s$ (or $\delta C-\ln s$) curves are similar in shape, but quantitatively, the total increase in δC through the distance range $1 < s \leq 600$ nm is quite sensitive to the tip radius. We denote this total capacitance change by $\Delta(\delta C)$. A blunt tip of $R \sim 4000$ nm gives $\Delta(\delta C) \sim 0.61$ fF. As the tip radius is reduced, $\Delta(\delta C)$ decreases with the tip radius and becomes 0.28 fF when $R \sim 2000$ nm. For a sharp tip of $R = 30$ nm, $\Delta(\delta C)$ is approximately 0.045 fF which is less than one tenth of that of the 4000 nm tip. In Fig. 4, the curves for $R \geq 2000$ nm were obtained with Pt-Ir tips and other curves with W tips. The observed tip dependence is, however, not due to the difference in the tip material since we obtained $\Delta(\delta C) \sim 0.4$ fF for an accidentally crushed W tip having an effective radius $R \sim 2100$ nm. This $\Delta(\delta C)$ is close to the value obtained with the Pt-Ir tip of the same tip radius. Therefore not the tip material but the tip geometry is the most relevant factor to the tip-sample capacitance and its gap dependence.

The results shown in Fig. 4 explain the large fluctuation in $\Delta(\delta C)$ observed in our previous experiments.^{35,36} Some tips give $\Delta(\delta C) \sim 0.1$ fF while others show $\Delta(\delta C) \sim 0.6$ fF. We suggested some tip effects but could not find out a specific correlation to the tip geometry. We can now understand that the changes in the tip radius give rise to the fluctuation in $\Delta(\delta C)$.

To obtain more quantitative information on the relation between the capacitance and the tip geometry, we have estimated the tip radius from the capacitance data. As mentioned in Sec. I, the capacitance between a sphere of radius

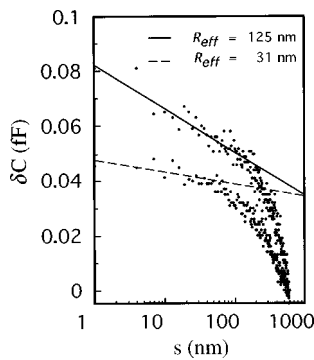


FIG. 5. $\delta C - \ln s$ curves for the $R = 124$ nm and the $R = 30$ nm tips. Solid and dashed lines represent a least-square fit to the data for $s < R$. From the slopes of these lines, R_{eff} defined by Eq. (1) can be calculated.

R and a plane has a logarithmic gap dependence $C = 2\pi\epsilon_0 R \ln(8R/s)$ when $s \ll R$.⁴ When plotted in a logarithmic distance scale, this sphere-plane capacitance would exhibit a straight line with a slope which is proportional to R . The experimental $\delta C - \ln s$ curves are not, however, linear as shown in Figs. 3 and 4. Therefore a simple spherical tip model with constant R cannot be applied to the experimental data. Nevertheless we can define an effective tip radius R_{eff} from the local slope of the measured $\delta C - \ln s$ curve as

$$R_{\text{eff}} = (d\delta C / d \ln s) / 2\pi\epsilon_0. \quad (1)$$

This R_{eff} changes with the distance s and can be compared with the real tip radius R determined from the SEM observation.

We first consider the capacitance curves acquired with sharp tips ($R \leq 100$ nm). Figure 5 shows two $\delta C - \ln s$ curves for the $R = 120$ nm and the $R = 30$ nm tips, respectively. A finer capacitance scale than that in Fig. 4(b) is used for showing the details. On this scale, one can see more clearly the shape of the $\delta C - \ln s$ curves and their apparent similarity to those obtained with blunt tips. When applying Eq. (1) to these capacitance curves, care must be taken to the fact that R_{eff} has the meaning of tip radius only at distances $s < R$. When $s > R$, the sphere-plane capacitance is not linear in $\ln s$ and R_{eff} defined by Eq. (1) is no longer related to the tip radius. Since the experimental range of s covers both $s < R$ and $s > R$ regimes for sharp tips, Eq. (1) should be applied only to the low- s part of the capacitance curves. Although the data fluctuation is magnified at this fine capacitance scale, it can be seen in Fig. 5 that the observed

$\delta C - \ln s$ curves show linear behavior at small distances. The solid and dashed lines in the figure represent the least square fit to the capacitance data satisfying the condition $s < R$. The R_{eff} values obtained from the slopes of these straight lines are 125 and 31 nm, respectively, which are in good agreement with each SEM tip radius. We applied the same fitting procedure to other $\delta C - \ln s$ curves and calculated R_{eff} . The results are summarized and compared with the SEM tip radius R in Table I. Because of the data fluctuation and the small number of data points, the estimated uncertainty in R_{eff} becomes relatively large for the 30 nm tip. Despite these uncertainties, the calculated R_{eff} values are in close agreement with R for all tips of $R \leq 100$ nm. This agreement between R_{eff} and R indicates that the observed gap dependence for sharp tips can be explained by the spherical tip model, at least at small distances $s < R$. On the other hand at $s > R$, the $\delta C - \ln s$ curves deviate from the fitted lines and show steeper slopes than predicted by the spherical tip model.

For blunt tips, the condition $s < R$ is satisfied over the entire experimental range of s , but the $\delta C - \ln s$ curves in Fig. 4(b) show no linear behavior at $s < R$. Therefore R_{eff} is not constant for blunt tips and changes with s . However, if we limit our attention to the approximately linear part of the $\delta C - \ln s$ plot at $s > 200$ nm, we can find that the slope of this part gives R_{eff} which is comparable to the SEM tip radius. The values of R_{eff} obtained from the capacitance data between 200 and 600 nm are also tabulated in Table I. We note that the value of R_{eff} is rather sensitive to the distance range used for the slope analysis and subjected to an uncertainty of about 20%. For blunt tips, the value of R also has a large uncertainty as mentioned in Sec. II. In spite of these uncertainties, the agreement between two tip radii is quite satisfactory. The spherical tip model is thus again partially valid at an intermediate distance range, $200 \text{ nm} < s \leq R$. In the proximity regime, $s < 50$ nm, the slope of the $\delta C - \ln s$ plot, or equivalently the effective tip radius R_{eff} , becomes too small to account for the SEM tip radius.

These findings reveal some differences between the capacitance-distance characteristics of sharp tips and that of blunt tips. In the case of sharp tips, the spherical tip model accounts for the measured δC at small gap distances but breaks down at large distances. The situation is just reversed for blunt tips: the spherical tip model is approximately valid at large distances but unable to predict the weak gap sensitivity of δC at small distances. The spherical tip model is thus valid in a limited distance range which changes with the tip radius. This result can be understood if we consider the field concentration to the tip apex. As the tip approaches the sample, the electric field becomes more concentrated in a small region just beneath the tip apex. Since the capacitance is proportional to the field flux, the dominant contribution to the tip-sample capacitance comes from the field-concentrated area which has a spatial extent comparable to the gap distance and shrinks with s . Therefore for sharp tips at small distances $s < R$, the high field region is mostly concentrated at the spherical tip apex, and the tip-sample capacitance behaves like a sphere-plane capacitance. Also the condition $s < R$ is the necessary condition for Eq. (1). These arguments explain why the R_{eff} values of sharp tips agree with the real

TABLE I. Comparison of the effective tip radius R_{eff} , calculated from the slope of the $\Delta C - s$ curve using Eq. (1), with the SEM tip radius R .

Tip	R_{eff} (nm)	R (nm)
W	31	30
W	41	60
W	77	60
W	100	100
W	125	120
Pt-Ir	2400	~2000
Pt-Ir	4600	~4000

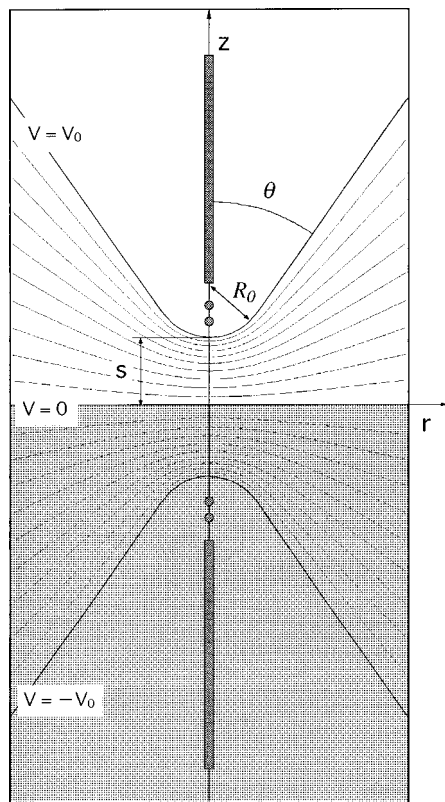


FIG. 6. In the image charge method, the tip-sample system is replaced by a set of point and segment charges placed on the tip axis (z axis), the ground plane at $z=0$ representing the sample, and the image charges at $z<0$, as illustrated in this figure. The strengths and the positions of these charges are optimized so that the equipotential surface at $V=V_0$ agrees with the tip surface. In our calculation, a truncated cone (half-cone angle θ) with a hemispherical cap (radius R_0) was employed as a model tip. The shaded bars and dots represent the segment and point charges, respectively, placed to simulate the tip geometry. The calculated equipotential surfaces are plotted in the figure.

tip radii. At $s > R$, the high field area starts to cover the nonspherical tip shank, and the capacitance deviates from sphere-plane capacitance. On the other hand on blunt tips at $s < 100$ nm, the size of the high field area is tens of nm and much smaller than the tip radius. On a nanometer scale, the surface of the blunt Pt-Ir tip is not spherical and has many small bumps as seen in Fig. 1(a). The field strength is then determined by these microroughnesses and, at $s < 50$ nm, focused to the most protruded asperity which effectively determines the capacitance. This situation is quite similar to the current focusing in STM imaging where the tunneling current is concentrated in an atom-sized “minitip” which determines the spatial resolution of STM. The suppressed slope of the $\delta C - \ln s$ curve at $s < 50$ nm, which gives $R_{\text{eff}} \sim 100$ nm, probably corresponds to the size of the asperity on the tip apex. As the gap distance increases, more coarse-scale roughness of the tip surface contributes to the capacitance. At $s > 200$ nm, the spherical geometry of the tip on a micrometer scale recovers the sphere-plane capacitance and gives $R_{\text{eff}} \sim R$, as shown in Table I. Due to the field concentration, the scale of the tip geometry relevant to the capacitance changes with the gap distance from hundreds of nm to

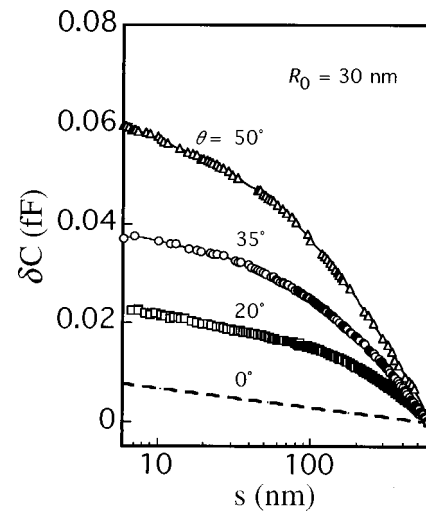


FIG. 7. Theoretical $\delta C - \ln s$ characteristics obtained for a model tip shown in Fig. 6. The tip radius R_0 is fixed to 30 nm and the half-cone angle θ is varied from 20° to 50° . Dashed line at $\theta=0^\circ$ represents the gap dependence of the sphere-plane capacitance.

~ 10 nm. The $\delta C - \ln s$ characteristics of sharp and blunt tips reflect the difference in their microscopic geometry at each scale.

IV. SIMULATION OF THE TIP-SAMPLE CAPACITANCE

As mentioned in Sec. III B, the spherical tip model explains only a part of the observed capacitance-distance characteristics. To understand the whole $\delta C - \ln s$ curves in Fig. 4(b) and their quantitative differences, we have to consider a more realistic tip geometry than a simple spherical tip. We here employed a simple “truncated cone + half sphere” tip and carried out a numerical calculation of the tip-sample capacitance and its gap dependence. The “truncated cone + half sphere” tip has been used by Mesa *et al.*³⁹ in their calculation of the field distribution around the tip. In this model, a tip is represented as a truncated cone of half-cone angle θ terminated with a half sphere of radius R_0 as shown in Fig. 6. More complex tip models such as the paraboloidal model and the hyperboloidal model are usually used to represent the tip geometry⁴⁰ since these models automatically satisfy the equipotential boundary condition on the tip surface. However, the equipotential surface changes with the tip-sample distance. As a result, a tip geometry which matches the equipotential surface at one distance cannot satisfy the boundary condition at the other distances. Therefore the paraboloidal and the hyperboloidal tip models have no advantages over our simple tip model when we calculate the gap dependence of the tip-sample capacitance. Another practical merit of the truncated cone + half sphere tip is that we can easily represent the tips of different sharpness by changing the half-cone angle θ . A tip with small R_0 and small θ represents a sharp tip, while the one with small R_0 but with large θ approximates a blunt tip having a protrusion at its apex. A more general method of representing nonsmooth tips with asperities has been proposed by Mesa and Sàenz.⁴¹ In our calcula-

tion, however, the simple truncated cone + half sphere model is sufficient for studying the capacitance changes with the tip geometry.

To calculate the tip-sample capacitance, we employed the image charge method developed by Mesa *et al.*³⁹ We place a tip at a distance s above a planar sample at $Z=0$ and define a cylindrical coordinate system as shown in Fig. 6. We also assume that the tip is biased at V_0 against the sample at $V=0$. Then we put a few point and segment charges on the tip axis (z axis), and calculate the potential distribution $V(r,z)$ in the gap region by superposing the contributions from these charges and also from their image charges behind the sample surface plane. The position and the magnitude of these charges are optimized so that the resulting $V(r,z)$ satisfies the equipotential boundary conditions on the tip surface [$V(r,z)=V_0$] and on the sample surface [$V(r,0)=0$]. An example of the potential distribution is displayed in Fig. 6. For capacitance calculation, we only need to know the field strength on the sample surface $-\partial V(r,z)/\partial z|_{z=0}$. By integrating $-\partial V(r,z)/\partial z|_{z=0}$ on the sample surface from $r=0$ to a cutoff radius r_c , we obtain the induced surface charge $-Q$ and the capacitance as $C=Q/V_0$.

Figure 7 shows a series of theoretical $\delta C - \ln s$ curves calculated for tips with $\theta=20^\circ$, 35° , and 50° . The radius of the hemispherical apex is fixed to $R_0=30$ nm, which is the smallest SEM tip radius used in our experiment. Six segment charges and four point charges were placed on the tip axis to generate the potential distribution. The cutoff radius was chosen as $r_c=10R_0$. As clearly seen in the figure, the calculated $\delta C - \ln s$ curves exhibit all features of the experimental $\delta C - \ln s$ curves in Fig. 4(b); the relatively rapid increase at $s>200$ nm and the weak gap dependence at smaller distances are well reproduced. The dashed line in Fig. 7 with $\theta=0^\circ$ represents the capacitance of a sphere of radius $R_0=30$ nm. Therefore the difference between the dashed line and other curves in Fig. 7 measures the contribution from the tip shank. We can see in the figure that the increase in capacitance at $s>200$ nm is mostly due to the capacitance of the tip shank. As s is reduced, the rate of increase in the capacitance is also reduced. At distances $s<50$ nm, all solid curves in Fig. 7 tend to show the same slope as that of the dashed line, indicating the transition from the shank-dominated capacitance to the apex-dominated capacitance. These results support our interpretation that the observed gap dependence of the capacitance reflects the process of field concentration to the tip apex.

It is noted in Fig. 7 that the total capacitance change $\Delta(\delta C)$ grows with the increase in cone angle θ . Since the large θ tip represents the blunt tip, this result corresponds well to the observed increase in $\Delta(\delta C)$ with the tip radius. Quantitatively, the calculated $\Delta(\delta C) \sim 0.038$ fF of a 35° tip is in reasonable agreement with the observed $\Delta(\delta C) \sim 0.045$ fF of the 30 nm tip. The value of $\Delta(\delta C)$ for a 50° tip is, however, about one-tenth of that of the 4000 nm tip. This quantitative discrepancy is due to the geometrical difference between our model tip and the blunt Pt-Ir tip. On the real tip surface, the area outside the protrusion has smaller curvature than the conical shank assumed in our model tip,

and thus gives larger capacitance contribution. As far as the blunt tips are concerned, a spherical tip with a small hemispherical protrusion on its surface, like the one used by Mesa and Sáenz,⁴¹ would give better quantitative results than the truncated cone + half sphere tip.

V. COMPARISON WITH PREVIOUS EXPERIMENTS

As mentioned in Sec. I, various capacitance-distance relations have been predicted in previous experiments. However, none of them are fully consistent with our capacitance data. For example, the inadequacy of the sphere-plane capacitance model used in SCaM⁴ has been already discussed in Sec. III B. Also the $1/s$ behavior obtained in the force microscopy¹¹ is not compatible with the convex curvature of the $\delta C - \ln s$ curves in Fig. 4(b). A possible explanation of this discrepancy is that the sensor tip used in the force microscopy has a flattened apex. Recently, the capacitance tip-sample force and its relation to the tip geometry has been studied in the atom-resolved AFM imaging of clean silicon surfaces.¹⁷ These kinds of experiments will give more detailed information on the gap dependence of the capacitive force.

In our previous experiments on the tip-semiconductor capacitance,^{35,36} we found that the relation $C=C_0-P_0s[1+\ln(D/s)]$ obtained for a conical tip¹⁴ is in good agreement with the observed gap dependence. Also in this experiment, the $\delta C - \ln s$ curves in Fig. 4(b) can be well fitted to this formula. Theoretically, the conical tip is the limiting case of the truncated cone + half sphere tip with no hemispherical cap ($R_0=0$). Therefore the success of the truncated cone + half sphere model discussed in Sec. IV explains the agreement between the conical tip model and the experimental results. However the real tip apex has a nonzero curvature which cannot be neglected at small distances. As a result, the formula $C_0-P_0s[1+\ln(D/s)]$, which saturates to C_0 as $s \rightarrow 0$, cannot account for the observed small but finite slope of the $\delta C - \ln s$ curve in Fig. 5. This breakdown of the conical tip model explains why we failed to obtain reasonable values for the fitting parameters P_0 and D as pointed out in Sec. III A.

Since our capacitance measurements do not extend to the tunneling regime, our experimental results cannot be fully compared with the Coulomb blockade and ultrafast STM experiments. Some Coulomb blockade experiments,^{21,22} however, provide capacitance data at large gap distances corresponding to conductances less than 1 nS. Since our initial tip position is at 1.7 nS, these capacitance data barely overlap with our capacitance measurements. At 1.7 nS, the Coulomb blockade capacitance takes 0.8–1.4 aF which is about 1/40 of the observed $\Delta(\delta C) \sim 45$ aF for the 30 nm tip. Also the $1/s$ behavior of the Coulomb blockade capacitance does not connect smoothly with the logarithmic gap dependence of δC at $s \ll R$. These discrepancies may not be unexpected if one assumes the “electro-chemical” capacitance^{31–33} in the Coulomb blockade, which is physically different from the geometrical capacitance measured in our experiment. As noted in Sec. I, however, the effective electrode area in the Coulomb blockade junction is determined by the size of the

charging island which is typically 10 nm or less. Since our results in Fig. 4(b) indicate the decrease in $\Delta(\delta C)$ with the tip radius, the small size of the island can explain the small junction capacitance in the Coulomb blockade, even without referring to the nongeometrical capacitance. We can therefore give no definite answer at present to the dual nature of the capacitance. Measurements of the geometrical capacitance at $s < 1$ nm will give some clue to this capacitance problem in the tunneling regime.

VI. CONCLUSION

We have studied the gap dependence of the tip-sample capacitance in the nontunneling regime and clarified the effects of tip geometry. We found that the capacitance and its gap sensitivity have an opposite gap dependence. The capacitance increases with the reduction of the gap distance, whereas the rate of capacitance change decreases with the gap distance. As a result, the capacitance shows a weak logarithmic gap dependence at small distances. Neither the $1/s$ divergence nor the nonclassical behavior is observed. Measurements on sharp and blunt tips revealed an appreciable influence of the tip geometry on the capacitance. First, the magnitude of the capacitance change depends on the tip geometry: blunt tips show larger capacitance changes than sharp tips. Second, the spherical tip model assuming the SEM tip radius accounts for the different part of the capacitance-distance characteristics, depending on the tip sharpness. For blunt tips, the spherical tip model is valid at large distances, while for sharp tips, the model predicts a correct tip radius only at small distances. All these findings can be consistently explained by considering the field concentration to the tip apex. The shrinkage of the high field region with the gap distance leads to a decrease in the effective tip radius in blunt tips and the dominance of the spherical apex in the capacitance of sharp tips. In both cases, the resulting capacitance-distance characteristics are in good agreement with our experimental observations. The capacitance calculation using the image charge method also provides quantitative support to this interpretation.

ACKNOWLEDGMENTS

This work was supported by a Grant-in-Aid for Scientific Research from the Ministry of Education, Science, and Culture of Japan.

¹J. R. Matey and J. Blanc, J. Appl. Phys. **57**, 1437 (1985).

²C. D. Bragg and P. J. King, J. Phys. E **21**, 147 (1988).

³C. C. Williams, W. P. Hough, and S. A. Rishton, Appl. Phys. Lett. **55**, 203 (1989).

⁴H. P. Kleinknecht, J. R. Sandercock, and H. Meier, Scanning Microsc. **2**, 1839 (1988).

⁵R. C. Barrett and C. F. Quate, J. Appl. Phys. **70**, 2725 (1991).

⁶M. Dreyer and R. Wiesendanger, Appl. Phys. A: Mater. Sci. Process. **61**, 357 (1995).

⁷H. Tomiye, H. Kawami, M. Izawa, M. Yoshimura, and T. Yao, Jpn. J. Appl. Phys., Part 1 **34**, 3376 (1995).

⁸J. J. Kopanski, J. F. Marchiando, and J. R. Lowney, J. Vac. Sci. Technol. B **14**, 242 (1996).

⁹N. Nakagiri, T. Yamamoto, H. Sugimura, and Y. Suzuki, J. Vac. Sci. Technol. B **14**, 887 (1996).

¹⁰C. J. Kang, C. K. Kim, J. D. Lera, Y. Kuk, K. M. Mang, J. G. Lee, K. S. Suh, and C. C. Williams, Appl. Phys. Lett. **71**, 1546 (1997).

¹¹Y. Martin, D. W. Abraham, and H. K. Wickramasinghe, Appl. Phys. Lett. **52**, 1103 (1988).

¹²J. E. Stern, B. D. Terris, H. J. Mamin, and D. Rugar, Appl. Phys. Lett. **53**, 2717 (1988).

¹³B. D. Terris, J. E. Stern, D. Rugar, and H. J. Mamin, Phys. Rev. Lett. **63**, 2669 (1989).

¹⁴H. Yokoyama, T. Inoue, and J. Itoh, Appl. Phys. Lett. **65**, 3143 (1994).

¹⁵R. M. Nyffenegger, R. M. Penner, and R. Schierle, Appl. Phys. Lett. **71**, 1878 (1997).

¹⁶T. Uchihashi, M. Ohta, Y. Sugawara, Y. Yanase, T. Shigematsu, M. Suzuki, and S. Morita, J. Vac. Sci. Technol. B **15**, 1543 (1997).

¹⁷M. Guggisberg, M. Bammerlin, R. Lüthi, Ch. Loppacher, F. M. Battiston, J. Lü, A. Baratoff, E. Meyer, and H.-J. Güntherodt, Appl. Phys. A: Mater. Sci. Process. **66**, S245 (1998).

¹⁸P. J. M. van Bentum, H. van Kempen, L. E. C. van de Leemput, and P. A. A. Teunissen, Phys. Rev. Lett. **60**, 369 (1988).

¹⁹R. Wilkins, E. Ben-Jacob, and R. C. Jaklevic, Phys. Rev. Lett. **63**, 801 (1989).

²⁰C. Schönenberger, H. van Houten, J. M. Kerkhof, and H. C. Donkersloot, Appl. Surf. Sci. **67**, 222 (1993).

²¹D. Anselmetti, T. Richmond, A. Baratoff, G. Borer, M. Dreier, M. Bernasconi, and H.-J. Güntherodt, Europhys. Lett. **25**, 297 (1994).

²²L. Wang, M. E. Taylor, and M. E. Welland, Surf. Sci. **322**, 325 (1995).

²³C. T. Black, M. T. Tuominen, and M. Tinkham, Phys. Rev. B **50**, 7888 (1994).

²⁴R. P. Andres, T. Bein, M. Dorogi, S. Feng, J. I. Henderson, C. P. Kubiak, W. Mahoney, R. G. Osifchin, and R. Reifenberger, Science **272**, 1323 (1996).

²⁵P. Radjkovic, M. Schwartzkopff, M. Enachescu, E. Stefanov, E. Hartmann, and F. Koch, J. Vac. Sci. Technol. B **14**, 1229 (1996).

²⁶F. Yamaguchi, D. Huang, and Y. Yamamoto, Jpn. J. Appl. Phys., Part 1 **36**, 3799 (1997).

²⁷S. Weiss, D. Botkin, D. F. Ogletree, M. Salmeron, and D. S. Chemla, Phys. Status Solidi B **188**, 343 (1995).

²⁸R. H. M. Groeneveld and H. van Kempen, Appl. Phys. Lett. **69**, 2294 (1996).

²⁹U. Keil, J. R. Jensen, and J. R. Hvam, J. Appl. Phys. **81**, 2929 (1997); Appl. Phys. Lett. **70**, 2625 (1997).

³⁰J. R. Jensen, U. Keil, and J. R. Hvam, Appl. Phys. Lett. **70**, 2762 (1997).

³¹M. Büttiker, H. Thomas, and A. Prêtre, Phys. Lett. A **180**, 364 (1993).

³²M. Büttiker, J. Phys.: Condens. Matter **5**, 9361 (1993).

³³T. Christen and M. Büttiker, Phys. Rev. Lett. **77**, 143 (1996).

³⁴Y. Akama, A. Sakai, and K. Sugihara (unpublished).

³⁵S. Kurokawa, M. Yuasa, Y. Hasegawa, and A. Sakai, Surf. Sci. **357–358**, 532 (1996).

³⁶A. Sakai, S. Kurokawa, and Y. Hasegawa, J. Vac. Sci. Technol. A **14**, 1219 (1996).

³⁷J. Bono and R. H. Good, Jr., Surf. Sci. **151**, 543 (1985).

³⁸S. Kurokawa and A. Sakai (unpublished).

³⁹G. Mesa, E. Dobado-Fuentes, and J. J. Sáenz, J. Appl. Phys. **79**, 39 (1996).

⁴⁰M. K. Miller, A. Cerezo, M. G. Hetherington, and G. D. W. Smith, *Atom Probe Field Ion Microscopy* (Oxford University Press, Oxford, 1996).

⁴¹G. Mesa and J. J. Sáenz, Appl. Phys. Lett. **69**, 1169 (1996).